

Differentiable Rendering for 3D Fluorescence Microscopy

Sacha Ichbiah Fabrice Delbary Hervé Turlier
 Center for Interdisciplinary Research in Biology, Collège de France
 CNRS, Inserm, PSL University, Paris, France
 herve.turlier@college-de-france.fr

Abstract

*Differentiable rendering is a growing field that is at the heart of many recent advances in solving inverse graphics problems, such as the reconstruction of 3D scenes from 2D images. By making the rendering process differentiable, one can compute gradients of the output image with respect to the different scene parameters efficiently using automatic differentiation. Interested in the potential of such methods for the analysis of fluorescence microscopy images, we introduce **deltaMic**, a microscopy renderer that can generate a 3D fluorescence microscopy image from a 3D scene in a fully differentiable manner. By convolving the meshes in the scene with the point spread function (PSF) of the microscope, that characterizes the response of its imaging system to a point source, we emulate the 3D image creation process of fluorescence microscopy. This is achieved by computing the Fourier transform (FT) of the mesh and performing the convolution in the Fourier domain. Naive implementation of such mesh FT is however slow, inefficient, and sensitive to numerical precision. We solve these difficulties by providing a memory and computationally efficient fully differentiable GPU implementation of the 3D mesh FT. We demonstrate the potential of our method by reconstructing complex shapes from artificial microscopy images. Eventually, we apply our renderer to real confocal fluorescence microscopy images of embryos to accurately reconstruct the multicellular shapes of these cell aggregates.*

1. Introduction

Fluorescence microscopy [42] has become the most widespread technique to image biological objects. In fluorescence microscopy, biological samples are made visible by attaching a fluorescent dye - or fluorophore - to the structure of interest. Then a laser excites the dye, which emits, in response, fluorescent light that goes through the optics of the microscope and is detected by a photosensitive sensor to produce a 2-dimensional image. In confocal microscopy, the focal plane is varied to generate a 3D volumetric image

composed of optical sections of the biological sample.

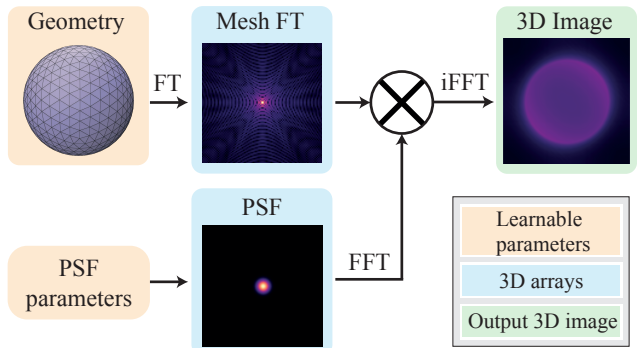


Figure 1. Overview of the differentiable fluorescence microscopy rendering pipeline. The renderer takes as input a triangle mesh, that represents the shape of a biological object, and a parameterized point spread function (PSF), that emulates the optics of the microscope, and outputs a 3D artificial microscopy image. By making every element of the pipeline differentiable, the gradients of the voxel image values with respect to the mesh geometry and PSF parameters can be computed efficiently with backpropagation. In turn, these gradients can be used to optimize input parameters to make the output image fit a real microscopy image.

In spite of the ubiquitous use of fluorescence microscopy in biology, extracting relevant quantitative information from 3D fluorescence images remains a major bottleneck, spurring the development of new methods. In recent years, researchers took inspiration from the field of computer vision, building in particular on the success of 2D convolutional neural networks (CNN) and adapting their architectures to the peculiarities of biological images [63, 11]. These deep learning (DL)-based tools for fluorescence imaging [3] have made it possible to perform or automate various image analysis tasks, including image restoration [71], instance segmentation [66, 68], or feature encoding with self-supervised learning [33]. However, the expressivity of neural networks also comes with drawbacks: CNNs are prone to feature "hallucinations" (i.e. detecting aberrant signal from noise), which is problematic for scientific research and medical applications, that cannot suffer from such er-

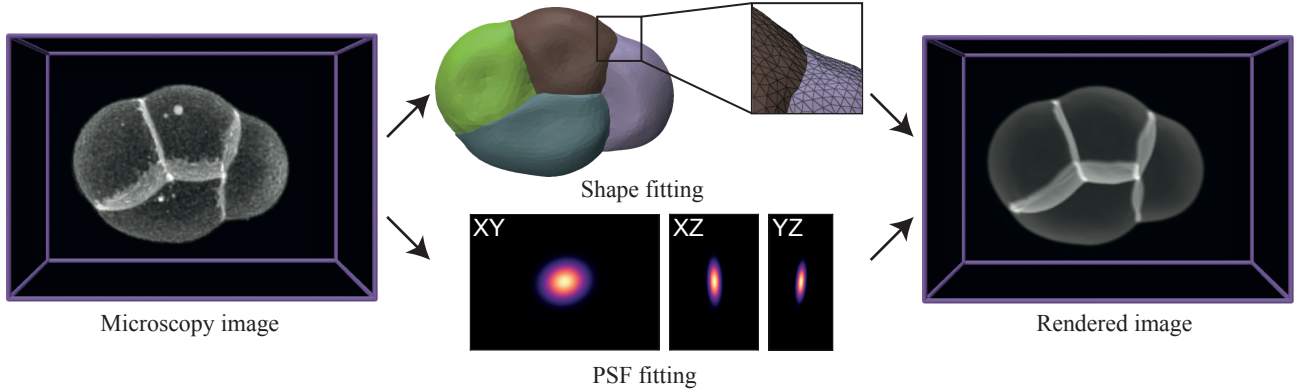


Figure 2. We apply our pipeline to learn both vertices position and PSF parameters from 3D confocal microscopy images.

rors. The goal of fluorescence microscopy is to identify one particular biological structure, which has generally a high degree of organization, such as lipid-membranes, cytoskeletal networks, or other organelles, by making them bright while keeping everything else dark. Therefore, except for unavoidable noise, fluorescence images are generally very sparse and made of well-structured objects such as points, filaments, surfaces or bulk solids. Because of this underlying simplicity, in parallel to the development of deep-learning based tools, one could witness in recent years a reverse trend in microscopy image analysis, going away from deep-learning, in favor of methods that rely on stronger prior knowledge [2, 39, 67].

Here, we demonstrate that differentiable rendering [29] stands out as a powerful approach to insert such priors for fluorescence image analysis: from defined parameters, such as parametrized shapes of objects and optical properties of the imaging system, one can approximate the image formation process. We introduce **deltaMic**, a differentiable renderer for 3D fluorescence microscopy images. Rendered images can be compared to true biological images using a voxel-based norm, and gradients of this loss with respect to input parameters can be determined efficiently with automatic differentiation. Minimizing this loss with a gradient-based optimization allows to fit the geometry of biological objects and to emulate the optical model of the microscope. Our renderer relies on an efficient and flexible framework to approximate the image formation process, that takes a mesh and a parameterized Point Spread Function (PSF) as inputs, and generates a volumetric image from them. To generate this 3D image, the mesh describing the geometry is convolved with the PSF via an element-wise product in the Fourier domain. We use distribution theory to express the Fourier Transform (FT) of a 2D shape embedded in 3D [27, 38], and derive the expression of the FT and its gradient in the case of a triangle mesh. We propose a narrow-band strategy to accelerate massively the computation of the mesh FT, and provide a

custom C++/CUDA implementation of both the forward and the backward passes that greatly enhances speed and memory efficiency. Our PyTorch implementation allows for gradients of the rendered 3D image values with respect to input parameters to be computed through automatic differentiation. We demonstrate the inverse-rendering capabilities of our pipeline by reconstructing the PSF and the complex shape of various objects and of early embryos from artificial and true fluorescence images. Importantly, we rely on previously developed approaches in the field of differentiable rendering to regularize the optimization problem [55].

Main contributions:

- We propose a simplified model of the fluorescence microscopy imaging process, combining an mesh description of objects geometry and a simple parameterized point spread function.
- We present a differentiable formulation of the Fourier transform of a triangle surface mesh, and its highly-optimized GPU implementation.
- We demonstrate the capacity of our differentiable renderer to reconstruct shapes from both artificial and real 3D microscopy images without the need for additional shape-regularization terms.

An open-source implementation of our method is available on <https://github.com/VirtualEmbryo/deltamic>

2. Related work

2.1. Point spread function models

The resolution of images seen with a fluorescence microscope are fundamentally limited by the diffraction of light [25]. If this response is invariant by translation, we can describe the imaging system by determining its PSF, that describes the response of the imaging system to a point source. Numerous physics-based models of PSFs have been devel-

oped [19, 35, 21, 22, 1], mostly for deconvolution applications [64]. The most straightforward way to determine a PSF is to directly generate microscopy images of tiny fluorescent beads that approximates a point source, and then fit the parameters of a given model to match this experimental PSF. In our approach, we decide to approximate the PSF by a Gaussian kernel, that is fully characterized by its covariance matrix. We note that our approach can be extended to learn parameters of more realistic PSF models, especially when vectorized implementations are available [40].

2.2. Artificial microscopy images generation

Creating artificial microscopy images has been the object of several studies, in order to evaluate image-analysis algorithms [60] and to create automatically annotated datasets for neural network training [51]. These works can be grouped into two families, with models that aims at reproducing the real image-formation process [13], and other approaches that uses texture synthesis [48, 72] or generative DL [24, 15] to make photorealistic images.

In [13], fluorophore distribution is defined via a boolean mask that indicates the presence or absence of fluorophores. This mask is subsequently convolved with a PSF provided by the user before adding camera noise. We follow and extend this approach, by giving a more accurate mathematical definition of the fluorophore density, that we define as a \mathbb{R}^3 -valued density.

2.3. Instance segmentation of fluorescent images

Biological image analysis is a subdomain of the broader field of computer vision, and state of the art segmentation methods in both fields followed the same historical evolution [49]: thresholding, watershed-transform [4, 5, 16] or optimization with graph-cuts [6] were the dominant segmentation techniques before the advent of deep-learning based pipelines [63, 11].

In 2D, the best results for the segmentation of biological objects have been obtained by using a large dataset of annotated images from varied sources to train a CNN to predict instance masks robustly and generically, being not bound to any particular biological samples nor imaging modalities [58, 34, 20]. Such approach could not yet be successfully reproduced in 3D, showing that DL-based volumetric data analysis is not just about extending 2D neural networks to 3D. 3D images, or Z-stacks, are obtained by stacking together 2D images by changing the position of the focal plane along the optical axis z , leading to large anisotropy along this spatial direction. This anisotropy is different for each imaging condition, leading to heterogeneous 3D datasets and making both the training and generalization of CNNs a daunting task. Limited GPU memory also poses large technical difficulties with current 3D biology images of typical size from 512^3 with a classical confocal micro-

scope to 2048^3 with latest light-sheet technologies.

2.4. Energy based segmentation

A large portion of the classical literature on image segmentation relies on the minimization of an energy functional $\mathcal{E}(\Lambda, m)$, that aims at modeling a distance between a desired shape Λ and a distinctive feature in the image m [52]. These features may be a sharp intensity gradient (using edge detectors [47]) or regions of largely different intensities [10]. To model the shape of objects, one can generally rely either on an implicit level-set or explicit mesh representation. The final shape Λ^* is obtained iteratively by gradient-based optimization of the functional. The opposite of the gradient $\frac{\partial \mathcal{E}(\Lambda, m)}{\partial \Lambda}$ can be interpreted as a force that moves the contour to the desired target shape, which has motivated the generic names of *snakes*, *active contours* [28] or *active meshes* [14] for such methods. One large drawback, it that these techniques most often require user-defined shape regularization terms (mechanically equivalent to global tension or bending energies) to penalize sharp features and obtain smooth shapes.

The peculiarity of fluorescent images of slender biological structures, such as membranes, is that the shape is defined by a thin region of high intensity immersed in the dark, which is not well-adapted for region-based or edge-based energies evoked earlier. Alternative approaches have directly defined a force based on the distance to the local maximum intensity in the image [45, 69]. Others have defined a proper energy functional as a distance between a microscopy image and an artificial image created from a mesh, as in [23, 54]. The artificial image is generated by creating a thin boolean mask from the mesh, that is then convolved with a PSF, that is assumed to be known. Our approach builds on these ideas but proposes a more rigorous, versatile and three-dimensional image rendering procedure, where we optimize both the mesh representing the shape and the PSF parameters together, without needing any explicit regularization terms to smooth the mesh.

2.5. Differentiable rendering

Rendering geometrical 2D or 3D shapes into raster (discrete) 2D images is an ubiquitous topic in computer graphics, and an increasing number of rendering frameworks are now made differentiable. This allows to solve inverse-rendering problems, where one can learn directly the parameters of a scene (shapes, textures, material properties) from single or multiple views of raster images [41, 56, 30]. In most cases, rasterization pipelines are not differentiable natively and discontinuities or occlusions can lead to incorrect gradients. A simple solution to soften sharp changes is to smoothen the image formation process with different strategies [61, 44, 36, 31].

Our fluorescence microscope renderer is based on mathematical operations that are differentiable by design, and does not need special adaptations to obtain meaningful gradients. Indeed, convoluting the mesh FT with a PSF naturally smoothes the image, in a similar manner as what is done for differentiable rasterization [44]. As for other frameworks, the number of parameters to optimize can be very high: a triangle mesh contains typically thousands of vertices, and a PSF can be parametrized by hundreds of parameters. Assuming all the building blocks of the models are constituted of differentiable operations, reverse-mode differentiation (also called backpropagation), based on the repeated use of the chain-rule, allows to compute efficiently partial derivatives with respect to any parameter. The efficiency and versatility of this method lead to the development of several libraries offering both GPU acceleration of classical automatic differentiation operations [59, 18] and a high level and memory efficient implementation of backpropagation. We built our pipeline in PyTorch [59] and provide our mesh FT as a differentiable function.

3. Rendering fluorescence microscopy images

Images are defined as intensity maps from $[0, 1]^3$ to \mathbb{R} without any loss of generality, as any non-cubic images can be linearly fitted in the cube $[0, 1]^3$. In the following, we will offer approximated descriptions of both the imaging system and the geometry of the biological samples, that will be combined to build our differentiable renderer.

3.1. Translation-invariant rendering model

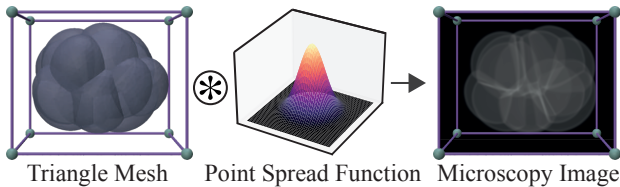


Figure 3. Principle of the rendering process. In our model, the fluorophores are distributed regularly on a surface Λ and the imaging system has a translation-invariant response function defined by the PSF. The microscopy image is created by convoluting the PSF with this uniform distribution of fluorophores.

We assume translation-invariance of the response function h of the fluorescence microscope. If so, a smooth image $u_\alpha : [0, 1]^3 \mapsto \mathbb{R}$ results from the convolution between a density of fluorophores $u_\Lambda : [0, 1]^3 \mapsto \mathbb{R}$ and a point spread function kernel $h : [0, 1]^3 \mapsto \mathbb{R}$:

$$u_\alpha(\mathbf{p}) = (u_\rho * h)(\mathbf{p}) = \int_{[0,1]^3} u_\Lambda(\mathbf{x})h(\mathbf{p} - \mathbf{x})d^3\mathbf{x}. \quad (1)$$

To avoid the computation of these integrals, we perform the convolution in the Fourier space by doing an element-

wise multiplication of the elements of the Fourier transforms \hat{u}_ρ and \hat{h} :

$$\hat{u}_\alpha = \hat{u}_\Lambda \cdot \hat{h}. \quad (2)$$

The biological structure of interest is made visible by fluorophores. The shape will thus be represented by u_Λ , whereas h should describe the response of the optical system to a point source. With this image formation model, one can start from a first guess (u_Λ^0, h^0) , and minimize the distance between the rendered image u_α^0 and a real microscopy image m . Doing so allows to learn both the geometry of the biological sample observed and the PSF of the imaging system, (u_Λ^*, h^*) . However, to learn meaningful representations, both of these elements have to be constrained by parametrized models that will implement our prior knowledge of the system.

3.2. Point spread-function model

The simplest PSF model is a Gaussian kernel. In this case the PSF is fully described by its covariance matrix $\Sigma \in \mathbb{R}^{3 \times 3}$:

$$h(\mathbf{z}) = \frac{e^{-\frac{1}{2}\mathbf{z}^T\Sigma^{-1}\mathbf{z}}}{\sqrt{(2\pi)^n \det \Sigma}}, \quad \mathbf{z} \in \mathbb{R}^3. \quad (3)$$

The FT \hat{h} of h is given by:

$$\hat{h}(\boldsymbol{\xi}) = e^{-\frac{1}{2}\boldsymbol{\xi}^T\Sigma^{-1}\boldsymbol{\xi}}, \quad \boldsymbol{\xi} \in \mathbb{R}^3. \quad (4)$$

In this framework, learning the PSF consists of learning all the coefficients of the covariance matrix Σ , and thus the level of blur of the rendered image. More photorealistic PSF based on a differentiable physical model could also be used [21, 22]. In that case, the learned parameters could be real optical parameters such as refraction indices or optical aberrations expressed using Zernike polynomials [37].

3.3. Geometrical models of biological objects

Extracting geometry from volumetric images consists of giving approximate representations of biological objects in terms of ND ($N = 0, 1, 2, 3$) discrete objects, embedded in a 3D space. They can be pretty diverse, both in terms of size and of topology. Here, we decide to focus on the lipid membranes that delimits cells and nuclei and to approximate them as 2D surfaces, that can be modeled efficiently with triangle meshes. Choosing the topology in such manner also implements prior knowledge: as we see in section 5.3, early embryos are composed of cells forming bounded regions that can be represented as a single non-manifold multimaterial mesh [46].

4. Fourier Transform of Surfaces

In this section, we will give an explicit expression of the FT for any 2D surfaces embedded in \mathbb{R}^3 , and give formulas of the FT and its gradient with respect to vertices position in the particular case of a triangle mesh.

4.1. Surfaces as spatial Dirac distributions

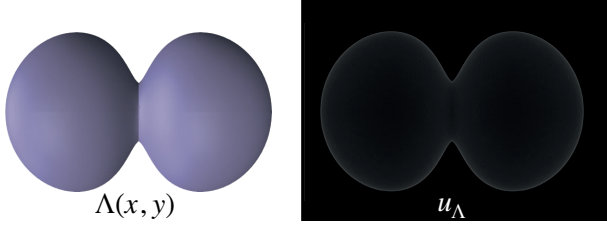


Figure 4. Surface Λ describing a dividing cell and its associated density u_Λ in \mathbb{R}^3 .

The density of fluorophores u_Λ will be equal to 1 only on an infinitely thin surface Λ , and 0 everywhere else.

To describe such irregular functions, one has to define them using spatial Dirac distributions. If we consider a surface given by a parameterization $\Lambda : [0, 1]^2 \rightarrow [0, 1]^3$, its spatial density is given by:

$$u_\Lambda = \frac{1}{|\Lambda|} \int_0^1 \int_0^1 \delta_\Lambda(x, y) a_\Lambda(x, y) dx dy, \quad (5)$$

where a_Λ is the surface element given by $a_\Lambda(x, y) = \|\partial_x \Lambda \times \partial_y \Lambda\|$, and $|\Lambda|$ is the total area of the surface Λ . The normalization by the total area ensures a density 1. When dealing with several surfaces with different densities, one has only to use a weighed sum of such u_Λ .

For all $\mathbf{z} \in \mathbb{R}^3$, the FT of the Dirac distribution at \mathbf{z} is given by:

$$\hat{\delta}_\mathbf{z}(\boldsymbol{\xi}) = e^{-i\mathbf{z} \cdot \boldsymbol{\xi}}, \quad \boldsymbol{\xi} \in \mathbb{R}^3. \quad (6)$$

Hence, the linearity of the FT gives:

$$\hat{u}_\Lambda(\boldsymbol{\xi}) = \frac{1}{|\Lambda|} \int_0^1 \int_0^1 a_\Lambda(x, y) e^{-i\Lambda(x, y) \cdot \boldsymbol{\xi}} dx dy. \quad (7)$$

4.2. The case of a triangulated surface

To describe surfaces Λ in practice, we will use triangle meshes. To compute the FT in this special case, as the FT is linear we just need to compute the FT of each triangle of the surface and sum their contributions.

4.2.1 Fourier transform and gradients for a triangle

We consider one triangle \mathcal{T} given by its vertices $(\mathbf{v}_1, \mathbf{v}_2, \mathbf{v}_3)$ and compute u_Λ and its spatial derivatives. We denote by $\mathbf{v}_4 = \mathbf{v}_1$ and similarly by $\mathbf{v}_0 = \mathbf{v}_3$. For $p = 1 \dots 3$, we define $p^- = p - 1$ and $p^+ = p + 1$ and denote by $\mathbf{e}_p = \mathbf{v}_{p^-} - \mathbf{v}_{p^+}$ the opposite edge to \mathbf{v}_p and by $l_p = |\mathbf{e}_p|$ its length. $A_\mathcal{T} = \frac{|\mathbf{e}_3 \times \mathbf{e}_1|}{2}$ denotes the area of the triangle, and $\mathbf{N}_\mathcal{T}$ denotes its unit normal given by: $\mathbf{N}_\mathcal{T} = \frac{\mathbf{e}_3 \times \mathbf{e}_1}{2A_\mathcal{T}}$. At last, for $p = 1 \dots 3$, we define $\mathbf{w}_p = \mathbf{e}_p \times \mathbf{N}_\mathcal{T}$, the non-normalized

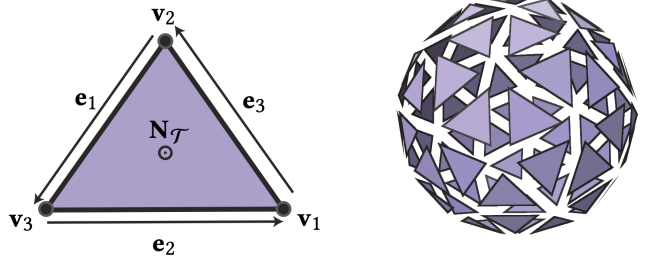


Figure 5. Notations for a triangle mesh. As the FT is linear, the FT of a single triangle will allow us to obtain the general expression of the FT for any triangle mesh.

outward normal to \mathcal{T} on the edge \mathbf{e}_p . For any p , we have:

$$\frac{\partial A_\mathcal{T}}{\partial \mathbf{v}_p} = -\frac{\mathbf{w}_p}{2}$$

If we define $\hat{u}_\mathcal{T}(\boldsymbol{\xi}) = \int_\mathcal{T} e^{-i\mathbf{z} \cdot \boldsymbol{\xi}} ds(\mathbf{z})$, then for all $\boldsymbol{\xi} \in \mathbb{R}^3$, we have:

$$\hat{u}_\mathcal{T}(\boldsymbol{\xi}) = 2A_\mathcal{T} f_\mathcal{T}(\boldsymbol{\xi}), \quad (8)$$

with $f_\mathcal{T}(\boldsymbol{\xi})$ defined by:

$$f_\mathcal{T}(\boldsymbol{\xi}) = \sum_{p=1}^3 \frac{e^{-i\mathbf{z}_p \cdot \boldsymbol{\xi}}}{(\mathbf{e}_{p^-} \cdot \boldsymbol{\xi})(\mathbf{e}_{p^+} \cdot \boldsymbol{\xi})}. \quad (9)$$

For all $p = 1 \dots 3$, we have:

$$\frac{\partial \hat{u}_\mathcal{T}}{\partial \mathbf{v}_p}(\boldsymbol{\xi}) = -f_\mathcal{T}(\boldsymbol{\xi}) \mathbf{w}_p + 2A_\mathcal{T} \frac{\partial f_\mathcal{T}(\boldsymbol{\xi})}{\partial \mathbf{v}_p}, \quad (10)$$

with:

$$\begin{aligned} \frac{\partial f_\mathcal{T}(\boldsymbol{\xi})}{\partial \mathbf{v}_p} = & \boldsymbol{\xi} \left[\frac{e^{-i\mathbf{z}_{p^+} \cdot \boldsymbol{\xi}}}{(\mathbf{v}_{p^-} \cdot \boldsymbol{\xi})^2 (\mathbf{v}_p \cdot \boldsymbol{\xi})} - \frac{e^{-i\mathbf{z}_{p^-} \cdot \boldsymbol{\xi}}}{(\mathbf{v}_p \cdot \boldsymbol{\xi}) (\mathbf{v}_{p^+} \cdot \boldsymbol{\xi})^2} \right. \\ & - \frac{i e^{-i\mathbf{z}_p \cdot \boldsymbol{\xi}}}{(\mathbf{v}_{p^-} \cdot \boldsymbol{\xi}) (\mathbf{v}_{p^+} \cdot \boldsymbol{\xi})} + \frac{e^{-i\mathbf{z}_p \cdot \boldsymbol{\xi}}}{(\mathbf{v}_{p^-} \cdot \boldsymbol{\xi})^2 (\mathbf{v}_{p^+} \cdot \boldsymbol{\xi})} \\ & \left. - \frac{e^{-i\mathbf{z}_p \cdot \boldsymbol{\xi}}}{(\mathbf{v}_{p^-} \cdot \boldsymbol{\xi}) (\mathbf{v}_{p^+} \cdot \boldsymbol{\xi})^2} \right]. \end{aligned} \quad (11)$$

4.2.2 Density for a triangle mesh

A triangle mesh is a surface $\Lambda = \{\mathcal{T}\}$ defined by a set of triangles. For $\boldsymbol{\xi} \in \mathbb{R}^3$, by linearity, its FT is defined by:

$$\hat{u}_\Lambda(\boldsymbol{\xi}) = \frac{\sum_{\mathcal{T} \in \Lambda} \hat{u}_\mathcal{T}(\boldsymbol{\xi})}{|\Lambda|} = \frac{\sum_{\mathcal{T} \in \Lambda} \hat{u}_\mathcal{T}(\boldsymbol{\xi})}{\sum_{\mathcal{T} \in \Lambda} A_\mathcal{T}}. \quad (12)$$

The gradient of the FT with respect to a vertex \mathbf{v} of the mesh is thus:

$$\frac{\partial \hat{u}_\Lambda(\boldsymbol{\xi})}{\partial \mathbf{v}} = \frac{1}{|\Lambda|} \left(\sum_{\mathcal{T} \in \mathbf{v}^*} \frac{\partial \hat{u}_\mathcal{T}(\boldsymbol{\xi})}{\partial \mathbf{v}} - \hat{u}_\Lambda(\boldsymbol{\xi}) \sum_{\mathcal{T} \in \mathbf{v}^*} \frac{\partial A_\mathcal{T}}{\partial \mathbf{v}} \right), \quad (13)$$

where \mathbf{v}_\star denotes the set of the triangles of Λ that contains the vertex \mathbf{v} .

4.2.3 Numerical approximations to avoid divergence

The FT of a Dirac distribution on a triangle is C^∞ . However, large computational errors arise when one denominator in the eq. (8) get close to zero. Error in rounding floating-point arithmetic leads to a limited numerical precision ϵ . Values smaller than this threshold ϵ cannot, in practice, be distinguished from 0. Therefore, when one term in denominator gets close to 0 in the expression (8) we replace it by an approximation that we describe in the following.

We write $f_T(\xi) = g(\mathbf{e}_1 \cdot \xi, \mathbf{e}_2 \cdot \xi, \mathbf{e}_3 \cdot \xi)$, with the function g defined for $(s, t, u) \in \mathbb{R}^3$ by

$$g(s, t, u) = \frac{-e^{is}}{(s-t)(s-u)} - \frac{e^{it}}{(t-u)(t-s)} - \frac{e^{iu}}{(u-s)(u-t)}. \quad (14)$$

When two values (a, b) among (s, t, u) are such that $|a - b| < \epsilon$, we obtain a value equal to 0 at the denominator and divergence. We solve this problem by deriving exact expressions of $g(s, t, u)$ in the case where $t=u$ or $t=s$ or $u=s$ or $u=s=t$, that replaces the original expression (14) when any (a, b) among (s, t, u) is such that $|a - b| < \epsilon$.

When only two values are too close from each other:

$$\begin{aligned} g(t, t, u) &= g(u, t, t) = g(t, u, t) \\ &= i \frac{e^{-it}}{t-u} + \frac{e^{-it}}{(t-u)^2} - \frac{e^{-iu}}{(t-u)^2}. \end{aligned} \quad (15)$$

When all three values are too close to each other, we replace the expression by

$$g(u, u, u) = \frac{e^{-iu}}{2}. \quad (16)$$

5. Experiments

5.1. Numerical implementation

5.1.1 Acceleration

The computation of the artificial image requires to compute the FT \hat{u}_Λ for each of the N voxels of the spatial grid and for each of the n_t triangles, with a runtime complexity of $\mathcal{O}(N \cdot n_t)$. The mesh FT gradient requires to compute a $\mathcal{O}(1)$ sum for each voxel, for each of the n_v vertices, leading to a complexity of $\mathcal{O}(N \cdot n_v)$. In practice, a 500^3 confocal microscopy picture has of 125 millions voxels, and a reasonable mesh will have $\approx 10^{3-4}$ vertices and triangles, leading to prohibitive computations times if this operation is not parallelized correctly. This high computational cost is a major restriction that has hampered the development of spectral methods in 3D, in spite of interesting potential applications [26].

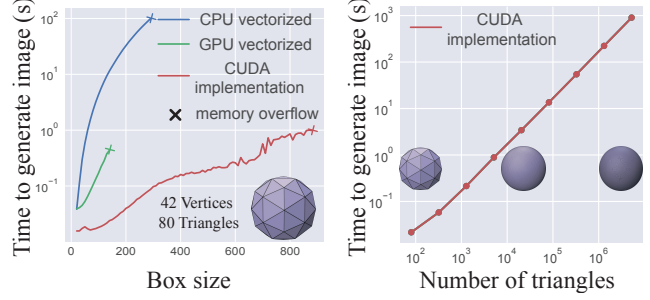


Figure 6. Benchmarking of the mesh FT computation. *Left* In a very small 80 triangles sphere, our custom CUDA implementation improves the speed and the memory efficiency of the mesh FT by several orders of magnitude. *Right* In a $[100]^3$ box, the forward pass of the mesh FT scales linearly with the number of triangles.

We propose two complementary strategies to accelerate the mesh FT: GPU parallelization and a narrow-band approximation method in the frequency domain.

GPU parallelization The grid-based structure of a 3D image makes its implementation naturally adapted to massively parallel computations on graphical processing units (GPU). We provide a custom CUDA implementation of the forward and the backward pass. As shown in figure 6, on a single NVIDIA V100 GPU, we obtain a $\approx 10^3$ speedup compared to the vectorized CPU implementation and we can perform computations with a far greater box size before overflow.

Narrow-band approximation in the frequency domain

As stated previously, the FT of the image is expressed as the element-wise product between the FT of the mesh and of the PSF: $\hat{u}_\alpha = \hat{u}_\Lambda \cdot \hat{h}$. Practically, our PSF acts as a low-pass filter, that will give more weight to low spatial frequencies of the mesh. A blurred image has a sparse PSF, with largest amplitudes for frequencies close to 0, therefore obliterating the fine details of the mesh. The more resolved the original biological image, the more frequencies in the PSF are needed to properly render it.

For any given spatial frequency ξ , if $\hat{h}(\xi) \approx 0$, one can spare the computation of $\hat{u}_\Lambda(\xi)$ as it will have negligible impact on the value of $\hat{u}_\alpha(\xi)$. In practice, we apply a cutoff in the frequency domain, and only compute the FT of the mesh for the frequencies for which the PSF is larger than 1% of its maximal value. For sparse PSFs, this spectral narrow-band method can reduce the computational cost by several orders of magnitude (table 1).

5.1.2 A staggered optimization scheme

In spite of all the speed improvements, computing the FT of the mesh and its gradient constitutes the computational

bottlenecks of our pipeline. We have two ways of computing the FT of the mesh: a fast and approximate way using the narrow-band method, and a slow and exact way by doing the full computation. The forward path is ≈ 10 times slower than the backward path, it is thus crucial to compute the backward path with the narrow-band method when possible. We decide therefore to decompose the coupled optimization problem into two optimization sub-problems, that are iterated in a staggered manner:

- Shape optimization:** To learn the shape, one does only need to compute the mesh FT approximately. We compute the approximate FT of the mesh using the narrow-band method, and make an optimization step for the vertex positions, without optimizing the PSF.
- PSF optimization:** To learn the point spread function, one need to know the value of the FT of the mesh in all the available frequencies, and should not be biased by the narrow-band frequency threshold that relies on the current values of the PSF. We compute the exact FT of the mesh, and make an optimization step for the PSF parameters, without optimizing the shape.

5.1.3 Shape optimization step

We optimize shapes by minimizing a modified L2 norm $\Phi_\kappa = ||u - m||^2 * m^\kappa$ with $\kappa = 1$, that removes external influence from dark regions of the original image m . Inspired by other works in differentiable rendering [55], we optimize vertex positions using AdamUniform and regularize gradient values by adding a diffusion term:

$$\mathbf{v} \leftarrow x - \eta(\mathbf{I} + \lambda\mathbf{L})^{-2} \frac{\partial \Phi_1}{\partial \mathbf{v}}, \quad (17)$$

where the Laplacian $\mathbf{L} \in \mathbb{R}^{n_v \times n_v}$ is a connectivity Laplacian defined on our triangle mesh, and $\lambda = 50$. Computing explicitly the inverse $(\mathbf{I} + \lambda\mathbf{L})^{-2}$ requires to use dense algebra, which can lead to prohibitive memory usage when the number of vertices n_v of the mesh grows. Instead, we solve the equivalent problem of finding the solution \mathbf{A} to $(\mathbf{I} + \lambda\mathbf{L})^{-2}\mathbf{A} = \frac{\partial \Phi_1}{\partial \mathbf{v}}$ with a sparse Cholesky decomposition [53, 55].

5.1.4 PSF optimization step

The optimization of PSF parameters aims at reproducing the whole image in details, for both light and dark regions. Minimizing the traditional L2 norm $\phi_0 = ||u - m||^2$ is therefore well-adapted to such task. We learn the correlation matrix Σ with the original Adam optimizer [32].

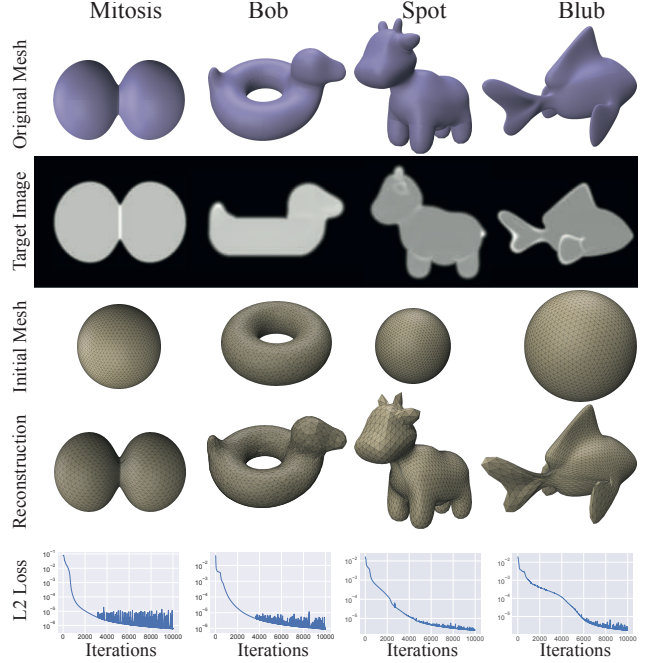


Figure 7. Surface mesh reconstruction from 3D artificial images. Artificial 3D images were created from triangle meshes using our renderer. Then, starting from spheres or toruses, we minimize the L2 norm between the rendered and the target images to reconstruct the original shape (see also supplementary videos 1-4).

5.2. Shape reconstruction from artificial images

We present in fig. 7 several examples of shape reconstruction from some classical meshes in computer graphics. Artificial images are generated with a Gaussian PSF characterized by an isotropic correlation matrix. Here, we focus on shape reconstruction and start directly from the target PSF correlation matrix Σ . Starting from meshes of elementary shapes (a sphere or a torus depending on the topology) we compute 10000 optimization steps for each example. Without any remeshing operation, our regularized shape optimization algorithm accurately converges to original shapes. Interestingly, in each of the four examples studied, the mesh converges with no collisions, although no collision detection or resolution method is implemented [8, 43].

5.3. Cell shape reconstruction and Gaussian PSF fitting on *C. elegans* embryo microscopy images

We use our method to fit shapes of cell clusters of *C. elegans* embryos, using 3D confocal microscopy images from [9]. The images are of size $205 \times 285 \times 134$. We describe cell clusters as non-manifold multimaterial meshes, as done in previous works [7], and we use a multimaterial mesh-based surface tracking method [12] to manage remeshing, collision detection and T1/T2 topology transition [70] operations. As first guesses, we generate foam-like multimaterial meshes with the correct number of cells by minimiz-

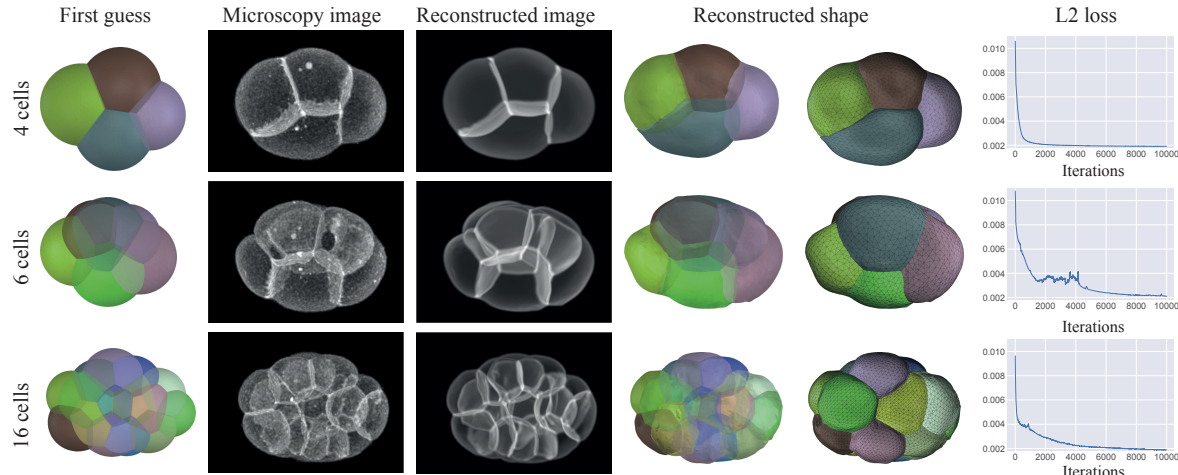


Figure 8. Shape reconstruction of *C. elegans* embryos. Starting from a foam ground truth, we optimize both vertices position and PSF parameters to recover individual cell shapes from real confocal microscopy data (see also supplementary videos 5-7).

Optimization step	forward (s)	backward (s)
PSF	0.001	0.004
Mesh (naive)	3.435	49.38
Mesh (ours)	1.757	17.04

Table 1. Average duration of the PSF and mesh optimization steps for the reconstruction described in section 5.3 with a naive implementation (naive) and with the spectral narrow-band approximation (**ours**). The mesh has 4000 vertices.

ing a surface energy at fixed cell volumes [46]. The resulting cell clusters are of roundish shapes with $\approx 4000 - 10000$ vertices that are subsequently optimized to fit true microscopy data. Here, we optimize jointly the PSF and the vertex positions in the mesh, following the strategy described in section 5.1.2. The duration of each step with a mesh of 4000 vertices is displayed in table 1. On both 4, 6 and 16 cells embryos, we predict individual cell shapes accurately after 10000 optimization steps, and the resulting reconstructed image is very close to the original microscopy image (fig. 8).

6. Conclusion

We have introduced **deltaMIC**, a differentiable fluorescence microscopy image renderer that takes a surface mesh and a parametrized PSF to generate realistic 3D confocal fluorescent images. The GPU-parallelized C++/CUDA implementation of the mesh FT allows to compute the forward and backward passes in tractable times, and is further optimized through a spectral narrow-band method. We demonstrate that our differentiable renderer can accurately retrieve fine details of complex shapes from artificial or real 3D microscopy fluorescent images, thanks to its ability to fine-tune the shape loss function via the PSF. Contrary to other

active-mesh segmentation methods, it does not require arbitrary shape regularization terms to achieve smooth results. Yet, other priors may be added to constrain shapes, based on physical or geometric knowledge, and could prove useful to solve inverse mechanical problems [17, 62].

Our method constitutes a fundamental building block for inverse rendering of 3D fluorescence microscopy images and paves the way for many applications. Extending our approach to 1D polygonal lines would allow to characterize the geometry of filaments in cytoskeletal networks, whose segmentation remain a major challenge [57]. Furthermore, our method shares several insights with deconvolution techniques for microscopy, which are fundamentally based on inverse image rendering and optimization [65]. Implementing more photorealistic PSF models based on specific microscope modalities [21, 22, 37] could allow performing blind deconvolution of microscopy images in an original manner. From an implementation perspective, and in spite of all the improvements proposed, the computational cost of our method remains a bottleneck for large 3D images, and other acceleration strategies would be explored. Eventually, it could be interesting to explore deep-learning based applications, where our renderer could be a differentiable building block of a larger pipeline, as in 2D applications [31, 50].

7. Acknowledgments

SI, FB and HT are supported by the CNRS and Collège de France. HT received funding from the European Research Council (ERC) under the European Union’s Horizon 2020 research and innovation programme (Grant agreement No. 949267). SI was funded by Ecole Polytechnique (AMX grant). We thank Baptiste Nicolet for insightful discussions, and H. Borja da Rocha and K. Crane for their meshes.

References

- [1] Matthew R. Arnison and Colin J.R. Sheppard. A 3d vectorial optical transfer function suitable for arbitrary pupil functions. *Optics Communications*, 211(1):53–63, 2002. 3
- [2] Joshua Batson and Loïc Royer. Noise2self: Blind denoising by self-supervision. In Kamalika Chaudhuri and Ruslan Salakhutdinov, editors, *Proceedings of the 36th International Conference on Machine Learning, ICML 2019, 9-15 June 2019, Long Beach, California, USA*, volume 97 of *Proceedings of Machine Learning Research*, pages 524–533. PMLR, 2019. 2
- [3] Chinmay Belthangady and Loic A Royer. Applications, promises, and pitfalls of deep learning for fluorescence image reconstruction. *Nature methods*, 16(12):1215–1225, 2019. 1
- [4] Serge Beucher. The watershed transformation applied to image segmentation. *Scanning Microscopy*, 1992(6):28, 1992. 3
- [5] Serge Beucher and Fernand Meyer. The morphological approach to segmentation: the watershed transformation. In *Mathematical morphology in image processing*, pages 433–481. CRC Press, 2018. 3
- [6] Yuri Boykov and Gareth Funka-Lea. Graph cuts and efficient nd image segmentation. *International journal of computer vision*, 70(2), 2006. 3
- [7] Kenneth A Brakke. The surface evolver. *Experimental mathematics*, 1(2):141–165, 1992. 7
- [8] Tyson Brochu, Essex Edwards, and Robert Bridson. Efficient geometrically exact continuous collision detection. *ACM Transactions on Graphics (TOG)*, 31(4):1–7, 2012. 7
- [9] Jianfeng Cao, Guoye Guan, Vincy Wing Sze Ho, Ming-Kin Wong, Lu-Yan Chan, Chao Tang, Zhongying Zhao, and Hong Yan. Establishment of a morphological atlas of the *Caenorhabditis elegans* embryo using deep-learning-based 4d segmentation. *Nature communications*, 11(1):1–14, 2020. 7
- [10] T.F. Chan and L.A. Vese. Active contours without edges. *IEEE Transactions on Image Processing*, 10(2):266–277, 2001. 3
- [11] Özgün Çiçek, Ahmed Abdulkadir, Soeren S. Lienkamp, Thomas Brox, and Olaf Ronneberger. 3d u-net: Learning dense volumetric segmentation from sparse annotation. In Sebastien Ourselin, Leo Joskowicz, Mert R. Sabuncu, Gozde Unal, and William Wells, editors, *Medical Image Computing and Computer-Assisted Intervention – MICCAI 2016*, pages 424–432, Cham, 2016. Springer International Publishing. 1, 3
- [12] Batty C. & Grinspun E. Da, F. Multimaterial mesh-based surface tracking. *ACM Trans. Graph.*, 33:112:1–112:11, 2014. 7
- [13] Serge Dmitrieff and François Nédélec. Confocalgn: A minimalistic confocal image generator. *SoftwareX*, 6:243–247, 2017. 3
- [14] Alexandre Dufour, Roman Thibeaux, Elisabeth Labruyere, Nancy Guillen, and Jean-Christophe Olivo-Marin. 3-d active meshes: fast discrete deformable models for cell tracking in 3-d time-lapse microscopy. *IEEE transactions on image processing*, 20(7):1925–1937, 2010. 3
- [15] Dennis Eschweiler, Malte Rethwisch, Mareike Jarchow, Simon Koppers, and Johannes Stegmaier. 3d fluorescence microscopy data synthesis for segmentation and benchmarking. *Plos one*, 16(12):e0260509, 2021. 3
- [16] Romain Fernandez, Pradeep Das, Vincent Mirabet, Eric Moscardi, Jan Traas, Jean-Luc Verdeil, Grégoire Malandain, and Christophe Godin. Imaging plant growth in 4d: robust tissue reconstruction and lineaging at cell resolution. *Nature methods*, 7(7):547–553, 2010. 3
- [17] Anna Frishman and Pierre Ronceray. Learning force fields from stochastic trajectories. *Physical Review X*, 10(2):021009, 2020. 8
- [18] Roy Frostig, Matthew Johnson, and Chris Leary. Compiling machine learning programs via high-level tracing. 2018. 4
- [19] Sarah Frisken Gibson and Frederick Lanni. Experimental test of an analytical model of aberration in an oil-immersion objective lens used in three-dimensional light microscopy. *J. Opt. Soc. Am. A*, 9(1):154–166, Jan 1992. 3
- [20] Miller-G. Moen E. et al. Greenwald, N.F. Whole-cell segmentation of tissue images with human-level performance using large-scale data annotation and deep learning. *Nat Biotechnol*, 40:555–565, 2022. 3
- [21] Bridget M. Hanser, Mats G. L. Gustafsson, David A. Agard, and John W. Sedat. Phase retrieval for high-numerical-aperture optical systems. *Opt. Lett.*, 28(10):801–803, May 2003. 3, 4, 8
- [22] B. M. Hanser, M. G. L. Gustafsson, D. A. Agard, and J. W. Sedat. Phase-retrieved pupil functions in wide-field fluorescence microscopy. *Journal of Microscopy*, 216(1):32–48, 2004. 3, 4, 8
- [23] Jo A. Helmuth and Ivo F. Sbalzarini. Deconvolving active contours for fluorescence microscopy images. In George Bebis, Richard Boyle, Bahram Parvin, Darko Koracin, Yoshinori Kuno, Junxian Wang, Jun-Xuan Wang, Junxian Wang, Renato Pajarola, Peter Lindstrom, André Hinkenjann, Miguel L. Encarnação, Cláudio T. Silva, and Daniel Com-ing, editors, *Advances in Visual Computing*, pages 544–553, Berlin, Heidelberg, 2009. Springer Berlin Heidelberg. 3
- [24] Reka Hollandi, Abel Szkalitsy, Timea Toth, Ervin Tasnadi, Csaba Molnar, Botond Mathe, Istvan Grexa, Jozsef Molnar, Arpad Balind, Mate Gorbe, Maria Kovacs, Ede Migh, Allen Goodman, Tamas Balassa, Krisztian Koos, Wenyu Wang, Juan Carlos Caicedo, Norbert Bara, Ferenc Kovacs, Lassi Paavola, Tivadar Danko, Andras Kriston, Anne Elizabeth Carpenter, Kevin Smith, and Peter Horvath. nucleaizer: A parameter-free deep learning framework for nucleus segmentation using image style transfer. *Cell Systems*, 10(5):453–458.e6, 2020. 3
- [25] Shinya Inoué. *Foundations of Confocal Scanned Imaging in Light Microscopy*, pages 1–19. Springer US, Boston, MA, 2006. 2
- [26] Chiyu Jiang, Dequan Wang, Jingwei Huang, Philip Marcus, Matthias Nießner, et al. Convolutional neural networks on non-uniform geometrical signals using euclidean spectral transformation. *arXiv preprint arXiv:1901.02070*, 2019. 6
- [27] Chiyu “Max” Jiang, Dequan Wang, Jingwei Huang, Philip Marcus, and Matthias Nießner. Convolutional neural networks on non-uniform geometrical signals using euclidean

- spectral transformation. In *7th International Conference on Learning Representations, ICLR 2019, New Orleans, LA, USA, May 6-9, 2019*. OpenReview.net, 2019. 2
- [28] Michael Kass, Andrew P. Witkin, and Demetri Terzopoulos. Snakes: Active contour models. *Int. J. Comput. Vis.*, 1(4):321–331, 1988. 3
- [29] Hiroharu Kato, Deniz Beker, Mihai Morariu, Takahiro Ando, Toru Matsuoka, Wadim Kehl, and Adrien Gaidon. Differentiable rendering: A survey, 2020. 2
- [30] Hiroharu Kato, Deniz Beker, Mihai Morariu, Takahiro Ando, Toru Matsuoka, Wadim Kehl, and Adrien Gaidon. Differentiable rendering: A survey. *CoRR*, abs/2006.12057, 2020. 3
- [31] Hiroharu Kato, Yoshitaka Ushiku, and Tatsuya Harada. Neural 3d mesh renderer. In *2018 IEEE Conference on Computer Vision and Pattern Recognition, CVPR 2018, Salt Lake City, UT, USA, June 18-22, 2018*, pages 3907–3916. Computer Vision Foundation / IEEE Computer Society, 2018. 3, 8
- [32] Diederik P Kingma and Jimmy Ba. Adam: A method for stochastic optimization. *arXiv preprint arXiv:1412.6980*, 2014. 7
- [33] Cheveralls K.C. Leonetti M.D. et al. Kobayashi, H. Self-supervised deep learning encodes high-resolution features of protein subcellular localization. *Nat Methods*, 19:995–1003, 2022. 1
- [34] Cheveralls K.C. Leonetti M.D. et al. Kobayashi, H. Self-supervised deep learning encodes high-resolution features of protein subcellular localization. *Nat Methods*, 19:995–1003, 2022. 3
- [35] Hal G. Kraus. Huygens–fresnel–kirchhoff wave-front diffraction formulation: spherical waves. *J. Opt. Soc. Am. A*, 6(8):1196–1205, Aug 1989. 3
- [36] Samuli Laine, Janne Hellsten, Tero Karras, Yeongho Seol, Jaakko Lehtinen, and Timo Aila. Modular primitives for high-performance differentiable rendering. *ACM Trans. Graph.*, 39(6), nov 2020. 3
- [37] Vasudevan Lakshminarayanan and Andre Fleck. Zernike polynomials: a guide. *Journal of Modern Optics*, 58(7):545–561, 2011. 4, 8
- [38] Shung-Wu Lee and R. Mittra. Fourier transform of a polygonal shape function and its application in electromagnetics. *IEEE Transactions on Antennas and Propagation*, 31(1):99–103, 1983. 2
- [39] Jaakko Lehtinen, Jacob Munkberg, Jon Hasselgren, Samuli Laine, Tero Karras, Miika Aittala, and Timo Aila. Noise2noise: Learning image restoration without clean data. In Jennifer G. Dy and Andreas Krause, editors, *Proceedings of the 35th International Conference on Machine Learning, ICML 2018, Stockholmsmässan, Stockholm, Sweden, July 10-15, 2018*, volume 80 of *Proceedings of Machine Learning Research*, pages 2971–2980. PMLR, 2018. 2
- [40] Jizhou Li, Feng Xue, and Thierry Blu. Fast and accurate three-dimensional point spread function computation for fluorescence microscopy. *J. Opt. Soc. Am. A*, 34(6):1029–1034, Jun 2017. 3
- [41] Tzu-Mao Li, Michal Lukáč, Michaël Gharbi, and Jonathan Ragan-Kelley. Differentiable vector graphics rasterization for editing and learning. *ACM Trans. Graph.*, 39(6), nov 2020. 3
- [42] Jeff W Lichtman and José-Angel Conchello. Fluorescence microscopy. *Nature methods*, 2(12):910–919, 2005. 1
- [43] Ming C Lin, Dinesh Manocha, and Young J Kim. Collision and proximity queries. In *Handbook of discrete and computational geometry*, pages 1029–1056. Chapman and Hall/CRC, 2017. 7
- [44] Shichen Liu, Tianye Li, Weikai Chen, and Hao Li. Soft rasterizer: A differentiable renderer for image-based 3d reasoning. In *Proceedings of the IEEE/CVF International Conference on Computer Vision (ICCV)*, October 2019. 3, 4
- [45] Mercier V. Chiaruttini N. Machado, S. Limeseg: a coarse-grained lipid membrane simulation for 3d image segmentation. *BMC Bioinformatics*, 20, 2019. 3
- [46] Jean-Léon Maître, Hervé Turlier, Rukshala Illukkumbura, Björn Eismann, Ritsuya Niwayama, François Nédélec, and Takashi Hiiragi. Asymmetric division of contractile domains couples cell positioning and fate specification. *Nature*, 536(7616):344–348, 2016. 4, 8
- [47] Ravi Malladi, James A Sethian, and Baba C Vemuri. Shape modeling with front propagation: A level set approach. *IEEE transactions on pattern analysis and machine intelligence*, 17(2):158–175, 1995. 3
- [48] Patrik Malm, Anders Brun, and Ewert Bengtsson. Simulation of bright-field microscopy images depicting pap-smear specimen. *Cytometry Part A*, 87(3):212–226, 2015. 3
- [49] Erik Meijering. Cell segmentation: 50 years down the road [life sciences]. *IEEE Signal Processing Magazine*, 29(5):140–145, 2012. 3
- [50] Ben Mildenhall, Pratul P. Srinivasan, Matthew Tancik, Jonathan T. Barron, Ravi Ramamoorthi, and Ren Ng. Nerf: Representing scenes as neural radiance fields for view synthesis. *CoRR*, abs/2003.08934, 2020. 8
- [51] Leonid Mill, David Wolff, Nele Gerrits, Patrick Philipp, Lasse Kling, Florian Vollnhals, Andrew Ignatenko, Christian Jaremenko, Yixing Huang, Olivier De Castro, et al. Synthetic image rendering solves annotation problem in deep learning nanoparticle segmentation. *Small Methods*, 5(7):2100223, 2021. 3
- [52] David Bryant Mumford and Jayant Shah. Optimal approximations by piecewise smooth functions and associated variational problems. *Communications on pure and applied mathematics*, 1989. 3
- [53] Maxim Naumov. Parallel solution of sparse triangular linear systems in the preconditioned iterative methods on the gpu. *NVIDIA Corp., Westford, MA, USA, Tech. Rep. NVR-2011*, 1, 2011. 7
- [54] Jeffrey P. Nguyen, Benjamin P. Bratton, and Joshua W. Shae-vitz. *Biophysical Measurements of Bacterial Cell Shape*, pages 227–245. Springer New York, New York, NY, 2016. 3
- [55] Baptiste Nicolet, Alec Jacobson, and Wenzel Jakob. Large steps in inverse rendering of geometry. *ACM Trans. Graph.*, 40(6), dec 2021. 2, 7
- [56] Merlin Nimier-David, Delio Vicini, Tizian Zeltner, and Wenzel Jakob. Mitsuba 2: A retargetable forward and inverse renderer. *ACM Trans. Graph.*, 38(6), nov 2019. 3

- [57] Bugra Özdemir and Ralf Reski. Automated and semi-automated enhancement, segmentation and tracing of cytoskeletal networks in microscopic images: A review. *Computational and Structural Biotechnology Journal*, 19:2106–2120, 2021. 8
- [58] Stringer C. Pachitariu, M. Cellpose 2.0: how to train your own model. *Nat Methods*, 19:1634–1641, 2022. 3
- [59] Adam Paszke, Sam Gross, Francisco Massa, Adam Lerer, James Bradbury, Gregory Chanan, Trevor Killeen, Zeming Lin, Natalia Gimelshein, Luca Antiga, Alban Desmaison, Andreas Köpf, Edward Yang, Zach DeVito, Martin Raison, Alykhan Tejani, Sasank Chilamkurthy, Benoit Steiner, Lu Fang, Junjie Bai, and Soumith Chintala. *PyTorch: An Imperative Style, High-Performance Deep Learning Library*. Curran Associates Inc., Red Hook, NY, USA, 2019. 4
- [60] Satwik Rajaram, Benjamin Pavie, Nicholas EF Hac, Steven J Altschuler, and Lani F Wu. Simucell: a flexible framework for creating synthetic microscopy images. *Nature methods*, 9(7):634–635, 2012. 3
- [61] Nikhila Ravi, Jeremy Reizenstein, David Novotný, Taylor Gordon, Wan-Yen Lo, Justin Johnson, and Georgia Gkioxari. Accelerating 3d deep learning with pytorch3d. *CORR*, abs/2007.08501, 2020. 3
- [62] Chloé Roffay, Chii J Chan, Boris Guirao, Takashi Hiiragi, and François Graner. Inferring cell junction tension and pressure from cell geometry. *Development*, 148(18):dev192773, 2021. 8
- [63] Olaf Ronneberger, Philipp Fischer, and Thomas Brox. U-net: Convolutional networks for biomedical image segmentation. In Nassir Navab, Joachim Hornegger, William M. Wells, and Alejandro F. Frangi, editors, *Medical Image Computing and Computer-Assisted Intervention – MICCAI 2015*, pages 234–241, Cham, 2015. Springer International Publishing. 1, 3
- [64] Daniel Sage, Lauréne Donati, Ferréol Soulez, Denis Fortun, Guillaume Schmit, Arne Seitz, Romain Guiet, Cédric Vonesch, and Michael Unser. Deconvolutionlab2: An open-source software for deconvolution microscopy. *Methods*, 115:28–41, 2017. 3
- [65] Pinaki Sarder and Arye Nehorai. Deconvolution methods for 3-d fluorescence microscopy images. *IEEE signal processing magazine*, 23(3):32–45, 2006. 8
- [66] Uwe Schmidt, Martin Weigert, Coleman Broaddus, and Gene Myers. Cell detection with star-convex polygons. In *Medical Image Computing and Computer Assisted Intervention - MICCAI 2018 - 21st International Conference, Granada, Spain, September 16-20, 2018, Proceedings, Part II*, pages 265–273, 2018. 1
- [67] Ahmet Can Solak, Loic A. Royer, Abdur-Rahmaan Janhangeer, and Hirofumi Kobayashi. royerlab/aydin: v0.1.15, Oct. 2022. 2
- [68] Wang T. Michaelos M. et al. Stringer, C. Cellpose: a generalist algorithm for cellular segmentation. *Nat Methods*, 18:100–106, 2021. 1
- [69] Wim Thiels, Bart Smeets, Maxim Cuvelier, Francesca Caroti, and Rob Jelier. spheresDT/Mpacts-PiCS: cell tracking and shape retrieval in membrane-labeled embryos. *Bioinformatics*, 37(24):4851–4856, 07 2021. 3
- [70] Denis L Weaire and Stefan Hutzler. *The physics of foams*. Oxford University Press, 2001. 7
- [71] Schmidt U. Boothe T. et al. Weigert, M. Content-aware image restoration: pushing the limits of fluorescence microscopy. *Nat Methods*, 15:1090–1097, 2018. 1
- [72] Veit Wiesmann, Matthias Bergler, Ralf Palmisano, Martin Prinzen, Daniela Franz, and Thomas Wittenberg. Using simulated fluorescence cell micrographs for the evaluation of cell image segmentation algorithms. *BMC bioinformatics*, 18(1):1–12, 2017. 3